Research Square

Preprints are preliminary reports that have not undergone peer review.
They should not be considered conclusive, used to inform clinical practice,
or referenced by the media as validated information.

Trim-Constrained Aero-Propulsive Assessment of Distributed Electric Ducted Fans for a Fixed-Wing Unmanned Aerial Vehicle

Agus Suprianto

agus137@brin.go.id

National Research and Innovation Agency

Firman Hartono

Bandung Institute of Technology

Agoes Moelyadi

Bandung Institute of Technology

Ariefa Yusabih

Bandung Institute of Technology

Nurhadi Pramana

National Research and Innovation Agency

Dana Herdiana

National Research and Innovation Agency

Sinung Tirtha Pinindriya

National Research and Innovation Agency

Angga Septiyana

National Research and Innovation Agency

Dede Santoso

National Research and Innovation Agency

Deasy Tresnoningrum

National Research and Innovation Agency

Amat Chaeroni

Universitas Suryadarma

Rinal Kharis

National Research and Innovation Agency

Novan Risnawan

National Research and Innovation Agency

Iqbal Reza Al Fikri

National Research and Innovation Agency

Research Article

Keywords: distributed electric propulsion, electric ducted fan, unmanned aerial vehicle, aero-propulsive integration, trim analysis, slipstream loading, powered wing

Posted Date: July 6th, 2026

DOI: https://doi.org/10.21203/rs.3.rs-10107317/v1

License: This work is licensed under a Creative Commons Attribution 4.0 International License. Read Full License

Additional Declarations: No competing interests reported.

Trim-Constrained Aero-Propulsive Assessment of Distributed Electric Ducted Fans for a Fixed-Wing Unmanned Aerial Vehicle

Agus Suprianto[1*], Firman Hartono[2†], Agoes Moelyadi[2†], Ariefa Yusabih[2†], Nurhadi Pramana[1†], Dana Herdiana[1†], Sinung Tirtha Pinindriya[1†], Angga Septiyana[1†], Dede Santoso[1†], Deasy Tresnoningrum[1†], Amat Chaeroni[3†], Rinal Kharis[1†], Novan Risnawan[1†], Iqbal Reza Al Fikri[1†]

[1*]National Research and Innovation Agency, South Tangerang, 15314, Indonesia.
[2]Bandung Institute of Technology, Bandung, 40132, Indonesia.
[3]Air Marshal Suryadarma Aerospace University, Jakarta, 13610, Indonesia.

*Corresponding author(s). E-mail(s): agus137@brin.go.id;
Contributing authors: firman.hartono@itb.ac.id; moelyadi.mochammad@gmail.com; ariefayusabih@gmail.com; nurh030@brin.go.id; dana006@brin.go.id; sinu002@brin.go.id; angg034@brin.go.id; dede026@brin.go.id; deas002@brin.go.id; achaeroni@unsurya.ac.id; rina016@brin.go.id; nova006@brin.go.id; iqba007@brin.go.id;
†These authors contributed equally to this work.

Abstract

Distributed electric propulsion (DEP) can improve the low-speed capability of fixed-wing unmanned aerial vehicles, but the same powered-flow mechanism can increase drag, alter spanwise loading, and reduce elevator authority. This paper presents a trim-constrained aero-propulsive framework for integrating twelve 70 mm electric ducted fans (EDFs) on the LSU 05 NG UAV. The novelty is not the isolated observation that slipstream increases lift, but the combined metric-level evaluation of lift augmentation, drag growth, aerodynamic-efficiency retention, and residual elevator margin within one conceptual-design workflow. A

reduced-order slipstream-loading model is used to screen the aircraft-level twelve-EDF layout, and a three-EDF geometry-resolved CFD workflow is prepared for paired power-off/power-on angle-of-attack assessment. The reduced-order results show 47.0-60.2% lift augmentation, 88.6-101.2% drag increase, and 16.15-24.32% degradation in lift-to-drag ratio. Cruise and takeoff remain trimmable, forward-CG landing becomes trim-limited, and all stall cases reach the elevator-deflection limit. The aft-CG case, $\boldsymbol{x_{CG}} = 0.37$ MAC, provides the best compromise among takeoff efficiency, landing trim margin, and vehicle-level feasibility.

Keywords: distributed electric propulsion, electric ducted fan, unmanned aerial vehicle, aero-propulsive integration, trim analysis, slipstream loading, powered wing

1 Introduction

Electrification changes fixed-wing UAV design from a propulsion-sizing problem into a coupled vehicle-integration problem. When electric propulsors are distributed along the wing, the propulsion system modifies the local velocity field, sectional lift, induced drag, pitching moment, and control-surface demand. Reviews of electric and hybrid-electric aircraft consistently emphasize that the aerodynamic value of DEP depends on integration with the airframe rather than motor efficiency alone [1–3]. NASA X-57 studies and recent DEP investigations further show that power-on effects should be evaluated at vehicle level because propulsor operation changes the aerodynamic state experienced by the wing and tail [4–6].

For small and medium UAVs, electric ducted fans are attractive because they are compact and can energize selected wing regions at low speed. However, a layout that increases CL may still be poor if it produces a disproportionate increase in CD, a non-elliptical spanwise loading distribution, or elevator saturation. Recent powered-wing, ducted-fan, and DEP-STOL studies demonstrate strong sensitivity to propulsor position, wake interaction, rotor loading, and high-lift configuration [7–20]. Stability studies also indicate that center-of-gravity (CG) position and tail authority can be as decisive as force coefficients in determining whether a configuration is usable [21–25].

The LSU 05 NG UAV is used here as a representative aerial-vehicle platform because its wing, tail, and high-lift airfoil provide a realistic integration environment for multiple EDFs. The research question is: how can the lift benefit of distributed EDF slipstream be assessed together with drag penalty and longitudinal trim feasibility during conceptual design? This question shifts the manuscript from a single-aircraft installation report toward a compact vehicle-level framework suitable for Vehicles: propulsion-induced aerodynamic gain is counted as useful only when efficiency and control authority remain acceptable. The contribution is threefold. First, the paper links slipstream velocity ratio, Gaussian EDF wake superposition, wing-force integration, and elevator trim in one reproducible workflow. Second, it reports lift gain, drag growth, lift-to-drag degradation, and residual elevator margin from the same reduced-order dataset rather than treating those metrics separately. Third, it provides a CFD

result-entry template for paired power-off/power-on simulations so that later ANSYS data can be inserted without changing the scientific structure of the paper.

Table 1 Condensed research gap and contribution relative to prior DEP and EDF studies.

Literature cluster	Remaining limitation	Contribution of this paper
DEP slipstream and powered-wing aerodynamics [11, 12, 17, 26, 27]	Lift increments are often discussed without a simultaneous trim-authority filter.	Couples lift augmentation with drag penalty and elevator residual margin.
Ducted-fan/EDF aerodynamics [7–10, 19, 28]	Fan-level thrust, torque, and wake data are not always connected to full-wing loading.	Links EDF-induced velocity to spanwise loading and aircraft-level coefficients.
UAV/eVTOL/DEP vehicle design [13, 15, 18, 20, 29, 30]	Conceptual studies may not expose CG-dependent control limits.	Screens $x_{\mathrm{CG}}/\mathrm{MAC} = 0.30$, 0.35, and 0.37 in the same trim model.
CFD and experimental aeropropulsive support [6, 12, 14, 31, 32]	Reduced-order studies can overstate CFD as validation when geometries do not match exactly.	Uses CFD as design-support evidence and separates validation from diagnostics.

2 Materials and Methods

2.1 Vehicle and DEP-EDF Configuration

The baseline platform is the LSU 05 NG fixed-wing UAV. The wing has a span of 5.5 m, planform area of 3.45 m^2, aspect ratio of 8.769, taper ratio of 0.603, and mean aerodynamic chord of 0.642 m. The main wing uses the FX 76-MP-160 airfoil, while the horizontal and vertical tailplanes use NACA 0012 sections. The DEP concept contains twelve 70 mm EDFs, with six units per semi-span. In the reduced-order layout, the EDF centers are distributed in the spanwise corridor $0.15 \leq \eta_j \leq 0.85$ and the chordwise station is treated as a design band, $0.60 \leq \frac{x_j}{c(y_j)} \leq 0.90$, rather than a fixed near-trailing-edge assumption.

2.2 Slipstream-Loading Model

The local slipstream velocity ratio is defined as

$$SVR(y) = \frac{V_{\mathrm{eff}}(y)}{V_\infty}. \tag{1}$$

The EDF-induced velocity increment is represented as a Gaussian superposition of the wakes generated by individual EDFs,

$$\Delta V_{\mathrm{slip}}(y) = \sum_{j=1}^{N_{\mathrm{EDF}}} k_j \sqrt{\frac{2T_j}{\rho A_j}} \exp\left(-\frac{(y-y_j)^2}{2\sigma_j^2}\right), \tag{2}$$

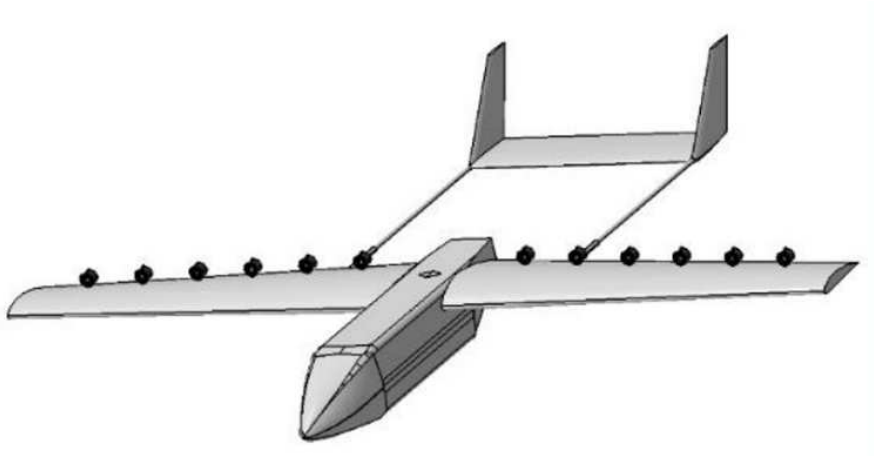


Fig. 1 LSU 05 NG with twelve EDF units distributed along the wing. The aircraft-specific geometry is used as a case study, while the analysis is framed in terms of general slipstream-loading and trim metrics.

Table 2 Compact configuration and operating-regime data.

Group	Parameter	Value
UAV	Mean take-off mass	102 kg
Wing	b_w, S_w, AR	5.5 m; 3.45 m^2; 8.769
Wing	c_r, c_t, taper ratio	0.73 m; 0.44 m; 0.603
Wing	MAC and airfoil	0.642 m; FX 76-MP-160
Tail	S_{HTP} and S_{VTP}	0.6603 m^2; 0.1610 m^2
DEP	EDF units	12 total, six per semi-span
DEP	D_j, R_j, A_j	70 mm; 35 mm; 3846.5 mm^2
DEP	Efficiencies	$\eta_{\text{motor}} = 92\%; \eta_{\text{fan}} = 80\%$
DEP	Slipstream parameters	$k_j = 0.7; \sigma_j = 1.2\,R_j; v_{exit}/V_\infty = 2.0; k_{ind} = 1.15$
Regimes	Cruise, takeoff, landing, stall	V_∞=25,22,21,19 m/s; $\alpha = 3°, 8°, 9°, 17°$
CG cases	x_{CG}/MAC	0.30, 0.35, 0.37

where T_j, A_j, y_j, σ_j, and k_j are the thrust, exit area, spanwise location, effective slipstream radius, and installation-loss factor of the j-th EDF. The effective local velocity and dynamic pressure are

$$V_{\text{eff}}(y) = V_\infty + \Delta V_{\text{slip}}(y), \tag{3}$$

$$q_{\text{local}}(y) = \frac{1}{2}\rho V_{\text{eff}}^2(y). \tag{4}$$

The spanwise lift coefficient is integrated using the local dynamic pressure and sectional lift response,

$$C_L = \frac{1}{q_\infty S_w} \int_{-b/2}^{b/2} q_{\text{local}}(y)\, c(y)\, C_l(y)\, dy, \tag{5}$$

and drag is evaluated with profile, induced, and installation-related components,

$$C_D = C_{D,0} + \frac{C_L^2}{\pi e AR} + \Delta C_{D_{\text{inst}}}. \tag{6}$$

This form is intentionally compact: it is not intended to replace high-fidelity CFD, but to expose the first-order consequences of EDF-induced dynamic-pressure redistribution.

2.3 Aero-Propulsive Trade-Off and Trim Metrics

Three nondimensional metrics are used to prevent a lift-only interpretation:

$$G_L = \frac{C_{L,\text{DEP}} - C_{L,0}}{C_{L,0}} \times 100\% \tag{7}$$

$$G_D = \frac{C_{D,\text{DEP}} - C_{D,0}}{C_{D,0}} \times 100\% \tag{8}$$

$$R_\eta = \frac{(C_L/C_D)_{\text{DEP}}}{(C_L/C_D)_0} \times 100\% \tag{9}$$

The longitudinal moment model is written as

$$C_M = C_{M_0} + C_{M_\alpha}\, \alpha + C_{M_{C_L}}\, C_L + C_{M_{\delta_e}}\, \delta_e \tag{10}$$

and the elevator deflection required for trim is

$$\delta_{e,\text{trim}} = -\frac{C_{M_0} + C_{M_\alpha}\, \alpha + C_{M_{C_L}}\, C_L}{C_{M_{\delta_e}}} \tag{11}$$

With $\delta_{e,\text{lim}} = -25°$, residual elevator authority is defined as

$$M_e = |\delta_{e,\text{lim}}| - |\delta_{e,\text{trim}}| \tag{12}$$

A case is classified as acceptable only when the efficiency loss remains tolerable and $M_e > 0$. This is a stricter criterion than reporting C_L augmentation alone.

2.4 CFD Result-Insertion Workflow

CFD results are inserted as a paired diagnostic dataset rather than as a formal validation of the twelve-EDF reduced-order model. The simulated configuration is a representative LSU 05 NG wing section equipped with three 70 mm EDF units. The post-processing uses $S_{ref} = 0.20895m^2, \rho = 1.0759kg/m, V_\infty = 15m/s$, and an active-rotor speed of 35,000 rpm, while the angle-of-attack sweep covers $\alpha = 0°,\ 5°,\ 10°,\ 12°,\ 15°,\ 17°,\ 19°,\ 20°$.

Table 3 CFD-supported wing-DEP assessment definition.

Item	Definition	Value
CFD role	Representative design-support assessment	Not formal validation of the reduced-order model
Geometry	LSU 05 NG wing/wing-section model with three EDFs	3 EDFs
Wing reference area	$S_{\mathrm{ref,CFD}}$	2.0895×10^5 mm^2 = 0.20895 m^2
EDF diameter	D_{EDF}	70 mm
Rotor-blade assembly surface area	$A_{\mathrm{rotor,DEP}}$	10,538 mm^2 per EDF
Freestream speed	V_∞	15 m/s
Angle-of-attack sweep	α_{CFD}	0, 5, 10, 12, 15, 17, 19, 20 deg
Power-off case	Rotors disabled	Wing-only reference
Power-on case	Three rotors active	35,000 rpm
Primary comparison	Power-on vs power-off at each α	Force, coefficient, thrust, torque, mass-flow, and power increments

The insertion workflow is intentionally comparative. For each α, the power-off case defines the baseline wing loading, whereas the power-on case quantifies the combined effect of thrust addition, slipstream acceleration, and wing–nacelle interference. The quantities transferred into the manuscript are $L, D, Y, C_L, C_D, C_L/C_D$, and the total EDF thrust. The decisive metrics are the signed increments $\Delta C_L, \Delta C_D$, and $\Delta(C_L/C_D)$, because they show whether DEP improves aerodynamic effectiveness or merely adds propulsive force and drag. On this basis, $\alpha = 5°$ is the most informative low-AoA case because it gives the largest positive efficiency gain, whereas$\alpha = 17°$ is the critical near-stall case because the efficiency increment becomes nearly zero and slightly negative in signed form.

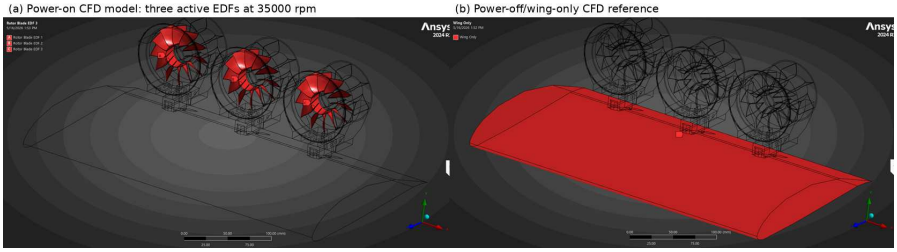


Fig. 2 Representative CFD model used for paired power-on and power-off assessment.

Accordingly, the CFD results should be reported as paired power-off/power-on values at identical α and then interpreted together with streamline-flow and pressure-contour visualisations. This sequence ties the quantitative increments to their flow-physics origin: attached-flow energisation at low α, progressive drag growth at intermediate α, and diminishing efficiency benefit close to stall. The associated rotor diagnostics comprise total thrust, total torque, mass-flow rate, shaft power, and diameter-based nondimensional EDF performance coefficients (C_T, C_Q, and C_P).

$$
\begin{aligned}
C_L^{\mathrm{CFD}} &= \frac{F_y}{q_\infty S_{\mathrm{ref,CFD}}} \\
C_D^{\mathrm{CFD}} &= \frac{|F_z|}{q_\infty S_{\mathrm{ref,CFD}}} \\
C_S^{\mathrm{CFD}} &= \frac{F_x}{q_\infty S_{\mathrm{ref,CFD}}} \\
T_\Sigma = \sum_{j=1}^{3} T_j, \quad Q_\Sigma &= \sum_{j=1}^{3} Q_j, \quad \dot{m}_\Sigma = \sum_{j=1}^{3} \dot{m}_j \\
C_T = \frac{T}{\rho n^2 D^4}, \quad C_Q &= \frac{Q}{\rho n^2 D^5}, \quad C_P = \frac{P}{\rho n^3 D^5} = 2\pi C_Q \\
P_{\mathrm{shaft},\Sigma} &= 2\pi n \sum_{j=1}^{3} |Q_j|
\end{aligned}
\tag{13}
$$

3 Results and Discussion

3.1 Reduced-Order Aero-Trim Results

The spanwise loading distribution explains why the DEP-EDF layout must be interpreted as a redistribution problem rather than a pure lift-increase problem. In the baseline condition, the wing loading follows the finite-wing and airfoil-polar response. When EDF slipstream is introduced, local lift peaks develop at the EDF stations, with valleys between adjacent wakes. This increases integrated lift, but it also moves the loading away from the smooth distribution that minimizes induced drag.

Across all regimes and CG cases, the twelve-EDF reduced-order configuration increases C_L by 47.0-60.2%, while C_D increases by 88.6-101.2%. The lift gain is therefore accompanied by a larger drag penalty, giving a 16.15-24.32% degradation in C_L/C_D. This behavior is physically consistent with propulsor-wing coupling: EDF wakes raise local dynamic pressure and lift, but the discrete wake pattern and installation drag increase profile and induced drag. The result is a useful powered-lift mechanism for low-speed operation, not a universal aerodynamic-efficiency improvement.

3.2 Longitudinal Trim and Center-of-Gravity Sensitivity

CG position has limited influence on the magnitude of slipstream-induced lift gain but strongly governs the elevator angle required for moment balance. The forward-CG case ($x_{\mathrm{CG}} = 0.30$ MAC) reaches the elevator limit in both landing and stall. The mid-CG case ($x_{\mathrm{CG}} = 0.35$ MAC) recovers a usable landing margin of 4.27° but still saturates in stall. The aft-CG case ($x_{\mathrm{CG}} = 0.37$ MAC) provides a 5.80° landing elevator margin and the lowest takeoff efficiency degradation (17.53%).

The aft-CG result does not imply that moving the CG aft is universally optimal, as excessive aft movement reduces the static stability margin. Rather, it demonstrates

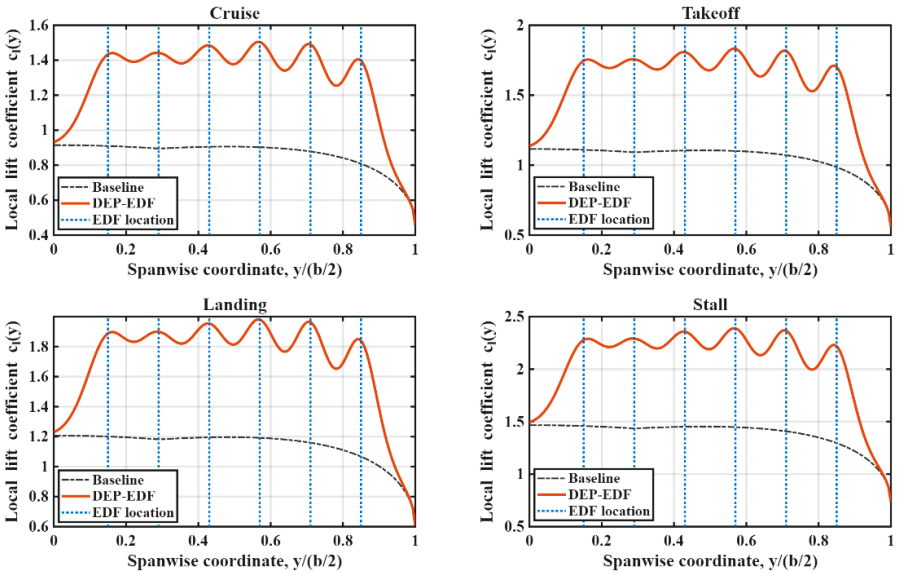


Fig. 3 Spanwise distribution of local lift coefficient for baseline and DEP-EDF configurations.

Table 4 Elevator trim and residual elevator authority.

Regime	x_{CG}/MAC	$\delta_{e,0}(deg)$	$\delta_{e,DEP}(deg)$	$M_e(deg)$	Status
Cruise	0.30	-13.60	-3.84	21.15	OK
Takeoff	0.30	-24.99	-22.91	2.08	OK
Landing	0.30	-24.99	-24.99	0.00	Limit
Stall	0.30	-24.99	-24.99	0.00	Limit
Cruise	0.35	-11.63	-0.07	24.92	OK
Takeoff	0.35	-24.99	-18.95	6.04	OK
Landing	0.35	-24.99	-20.72	4.27	OK
Stall	0.35	-24.99	-24.99	0.00	Limit
Cruise	0.37	-10.83	+1.43	23.56	OK
Takeoff	0.37	-24.99	-17.54	7.45	OK
Landing	0.37	-24.99	-19.19	5.80	OK
Stall	0.37	-24.99	-24.99	0.00	Limit

that DEP design must incorporate a CG envelope analysis and tail-authority constraint from the earliest conceptual design stage, extending the conclusions of prior stability studies [14, 22, 25] by explicitly mapping DEP-induced efficiency degradation alongside elevator saturation.

The trim response is the main vehicle-level discriminator. CG position has limited influence on the slipstream-induced lift increment, but it strongly changes the elevator deflection required to balance the pitching moment. Forward-CG landing reaches the elevator limit, while mid- and aft-CG landing recover positive margin. All stall cases remain elevator-limited, which means that the powered-lift benefit cannot be used safely without tail, CG-envelope, elevator-effectiveness, or thrust-scheduling changes.

Table 5 Reduced-order aircraft-level aero-trim metrics.

Regime	x_{CG}/MAC	$C_{L,DEP}$	$C_{D,DEP}$	G_L (%)	G_D (%)	$\Delta(C_L/C_D)$ (%)	M_e (deg)	Status
Cruise	0.30	1.288	0.086	60.2	91.1	16.15	21.15	OK
Takeoff	0.30	1.509	0.139	53.8	95.8	21.56	2.08	OK
Landing	0.30	1.636	0.163	51.6	101.2	24.32	0.00	Limit
Stall	0.30	2.080	0.282	47.0	89.3	22.18	0.00	Limit
Cruise	0.35	1.309	0.086	60.0	95.5	18.27	24.92	OK
Takeoff	0.35	1.535	0.137	56.5	93.0	18.60	6.04	OK
Landing	0.35	1.662	0.160	54.0	97.5	21.70	4.27	OK
Stall	0.35	2.080	0.282	47.0	89.3	22.18	0.00	Limit
Cruise	0.37	1.318	0.086	60.0	100.0	19.17	23.56	OK
Takeoff	0.37	1.545	0.136	57.5	91.5	17.53	7.45	OK
Landing	0.37	1.673	0.159	55.2	96.3	20.69	5.80	OK
Stall	0.37	2.080	0.281	47.0	88.6	22.18	0.00	Limit

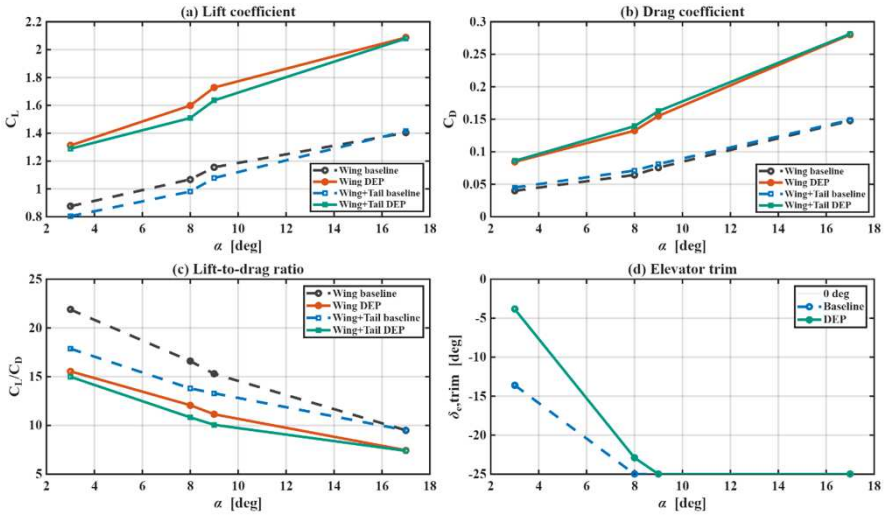


Fig. 4 Integrated aerodynamic coefficients and elevator trim response used to identify trim-limited DEP operation.

The best compromise in the present dataset is $x_{CG} = 0.37$ MAC.. It retains 5.80 deg of landing elevator margin, provides the smallest takeoff C_L/C_D degradation of 17.53%, and remains trimmable in cruise, takeoff, and landing. This does not imply that an aft CG is universally optimal, because excessive aft movement can reduce static stability margin. The more general conclusion is that DEP-EDF design must include the CG envelope and elevator authority at the beginning of conceptual design, not after the powered-wing layout has already been selected.

3.3 CFD Parameter Output using ANSYS Post-Processing

The ANSYS post-processing output confirms that DEP influence must be judged from paired increments rather than from absolute power-on forces alone. Table 6

summarises the aerodynamic coefficients for the wing under power-off and power-on conditions, while Table 7 reports the integrated rotor diagnostics and diameter-based nondimensional EDF performance coefficients. Figures 5–9 translate these tabulated values into force/coefficient trends and into two representative flow-visualisation pairs at $\alpha = 5°and\alpha = 17°$.

Table 6 Power-off and power-on aerodynamic coefficients for the wing DEP-EDF configuration.

α (deg)	$C_{L,\mathrm{off}}^{\mathrm{CFD}}$	$C_{D,\mathrm{off}}^{\mathrm{CFD}}$	$C_{L,\mathrm{on}}^{\mathrm{CFD}}$	$C_{D,\mathrm{on}}^{\mathrm{CFD}}$	ΔC_L (%)	ΔC_D (%)	$\Delta(C_L/C_D)$ (%)	Flow note
0	-0.1527	0.1448	-0.0100	0.3942	93.5	172.2	97.6	Attached/low AoA
5	0.0323	0.1307	0.2576	0.3760	697.5	187.7	177.2	Attached/low AoA
10	0.1179	0.1759	0.3762	0.4133	219.1	134.9	35.8	Intermediate loading
12	0.1516	0.1888	0.4483	0.5035	195.7	166.7	10.9	Intermediate loading
15	0.2573	0.2614	0.4958	0.6198	92.7	137.1	18.7	High lift
17	0.2285	0.2842	0.5485	0.6951	140.04	144.6	1.9	Near stall
19	0.2558	0.3190	0.3700	0.6981	44.6	118.8	33.9	Near/post stall
20	0.2391	0.3074	0.3378	0.7184	41.3	133.7	39.5	Near/post stall

Table 7 Integrated rotor diagnostics and diameter-based nondimensional EDF performance coefficients for the three active EDFs.

α (deg)	ΣT (N)	ΣQ (N m)	Σm (kg/s)	P_{shaft} (W)	C_T	C_Q	C_P
0	15.2107	0.4318	0.0012069	1581.827	0.0438	0.0178	0.1117
5	14.8532	0.24701	0.0007772	904.879	0.0428	0.0102	0.0639
10	14.0695	0.4618	0.0003667	1691.727	0.0405	0.0190	0.1194
12	13.1360	0.3915	0.0010709	1434.195	0.0379	0.0161	0.1013
15	12.4657	0.2816	0.0019701	1031.595	0.0359	0.0116	0.0728
17	10.9742	0.4664	0.0045632	1708.579	0.0316	0.0192	0.1206
19	10.1197	0.4772	0.0255551	1748.143	0.0292	0.0196	0.1234
20	10.0074	0.4967	0.0024515	1819.578	0.0288	0.0204	0.1285

Figure 5 shows that power-on operation increases lift throughout the AoA sweep, but it also produces a substantial drag penalty. Total EDF thrust decreases from 15.21 N at $\alpha = 0°to10.01Nat\alpha = 20°$, indicating progressively less favourable inflow alignment as the incidence increases. The side-force response remains negative and becomes larger in magnitude in the power-on condition, which is consistent with stronger local flow turning and nacelle–wing interaction. Figure 6 and Table 6 show the non-dimensional aerodynamic response. At $\alpha = 5°, C_L$ rises from 0.0323 to 0.2576, whereas C_D rises from 0.1307 to 0.3760. Because the baseline $C_Lat5°$ is still very small, the relative lift increment reaches +697.5%, and the aerodynamic efficiency improves from $C_L/C_D = 0.2471to0.6851, i.e., +177.2\%$. This is the clearest evidence that DEP

is most beneficial in the attached-flow regime: the powered slipstream raises lift much faster than the associated drag penalty.

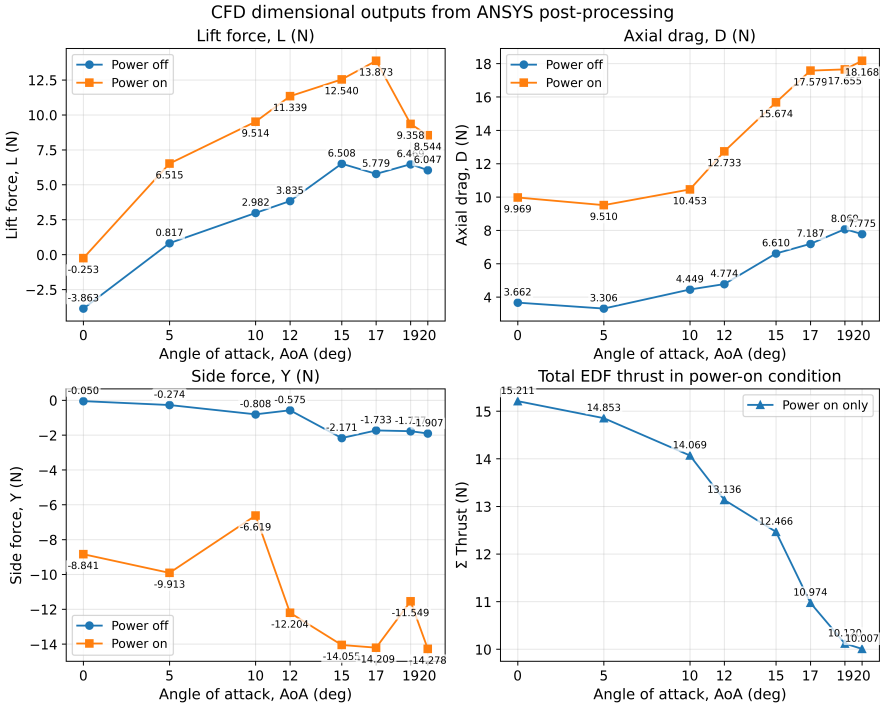


Fig. 5 CFD dimensional outputs from ANSYS post-processing. Power-on operation increases lift over the full AoA sweep, but the drag penalty and the decreasing total EDF thrust with increasing AoA demonstrate that the benefit is not uniform across the envelope.

At intermediate angles, the lift gain remains substantial, but the efficiency gain collapses rapidly. The power-on increments are still $+219.1\%$ in $C_L at \alpha = 10° and +195.7\% at \alpha = 12°$; however, the corresponding efficiency gains drop to $+35.8\%$ and $+10.9\%$. By $\alpha = 15°, C_L$ remains much larger in the power-on condition (0.4958 versus 0.2573), yet the efficiency improvement is limited to $+18.7\%$, showing that the drag penalty is becoming progressively dominant.

The critical near-stall behaviour appears at $\alpha = 17°$. Power-on operation still raises C_L from 0.2285 to 0.5485 and C_D from 0.2842 to 0.6951; however, C_L/C_D changes from 0.8041 to 0.7892. In signed form this corresponds to $\Delta(C_L/C_D) = 1.86\%$, although Table 6 lists the absolute magnitude as 1.9%. Thus, at 17° the DEP system no longer improves aerodynamic efficiency: the extra lift is almost exactly cancelled by the drag growth. The same tendency becomes stronger at $\alpha = 19° and 20°$, where the signed efficiency changes are 33.9% and 39.5%, confirming that the powered-wing benefit is exhausted in the near/post-stall regime.

Figure 8 explains why $\alpha = 5^\circ$ is the most favourable case. In the power-on streamline field, the EDF jets re-energise the local boundary layer and direct higher-momentum flow over the wing upper surface. The corresponding pressure contour indicates stronger suction and more effective loading over the wing region influenced by the three fans. The flow therefore remains predominantly attached, so the added momentum is converted into useful lift augmentation rather than into a pure drag penalty.

Figure 9 explains the opposite tendency at $\alpha = 17^\circ$. The power-on streamline pattern still contains strong jet momentum, but it is accompanied by more severe wake distortion, recirculation, and interaction losses around the nacelle–rotor system and near the aft wing region. The pressure contour remains altered by the EDF slipstream, yet the load increase is offset by a much larger drag penalty. In other words, the flow is no longer momentum-limited but separation-limited, so DEP adds force without providing a net efficiency benefit.

Taken together, the CFD dataset establishes a clear design message for the LSU 05 NG wing section at $V_\infty = 15$ m/s and 35,000 rpm. DEP is most effective as a low-to-moderate AoA lift-augmentation mechanism, not as a high-AoA stall-cure strategy. For the final manuscript, the most defensible emphasis is therefore the contrast between the strong low-AoA benefit at $\alpha = 5^\circ$ and the essentially neutral efficiency response at $\alpha = 17^\circ$, because this pair captures the operational limit of the present DEP arrangement.

3.4 Deep Research Synthesis and Design Implications

The reduced-order results and the CFD-entry workflow support a tiered research methodology. The reduced-order model is most useful for rapid screening of EDF spacing, CG location, chordwise placement, and trim feasibility. CFD is then used to interrogate the physical origin of the screened result: local separation, wake mixing, EDF-wing interference, and asymmetry. Experiments should follow after the design space is narrowed, beginning with EDF-only thrust-stand data and then a powered-wing wind-tunnel campaign.

This tiered approach responds directly to the literature gap. Compared with powered-wing studies that emphasize lift increments, the present framework adds a control-authority filter. Compared with fan-performance studies, it links EDF diagnostics to wing loading and trim. Compared with UAV conceptual-design studies, it exposes why the best design is not the maximum-lift case, but the case that preserves usable C_L/C_D and elevator margin. For the LSU 05 NG dataset, the six-EDF-per-semi-span layout is promising for lift augmentation but costly in drag and sensitive to CG. Future optimization should therefore smooth the spanwise blowing distribution, treat chordwise EDF placement as a design variable, and schedule EDF rpm with elevator trim and CG state.

4 Conclusions

This paper presents a compact trim-constrained aero-propulsive framework for distributed EDF integration on a fixed-wing UAV. Applied to the LSU 05 NG case,

the twelve-EDF reduced-order model produces 47.0-60.2% lift augmentation, but also 88.6-101.2% drag increase and 16.15-24.32% degradation in lift-to-drag ratio. These results show that powered lift cannot be evaluated using C_L alone.

The trim analysis identifies CG position and elevator authority as decisive vehicle-level constraints. Cruise and takeoff are trimmable for the evaluated cases, but forward-CG landing reaches the elevator limit and all stall cases saturate. The aft-CG case, $x_{CG} = 0.37$ MAC, gives the most balanced solution among the tested cases, retaining 5.80 deg of landing margin and the lowest takeoff efficiency degradation. The CFD templates provide a structured path for inserting final power-off/power-on ANSYS results at eight angles of attack. The next research step is to combine the completed CFD database with EDF thrust-stand measurements, powered-wing wind-tunnel testing, and flight-test trim data.

Acknowledgements

The authors thank the National Research and Innovation Agency, Indonesia, Bandung Institute of Technology, and Air Marshal Suryadarma Aerospace University for research collaboration and technical support in the development of the DEP-EDF configuration for the LSU 05 NG UAV platform.

Declarations

- Funding This research was funded by the National Research and Innovation Agency, Indonesia, through the Chairman of Research Organization for Aeronautics and Space under letter No. 1/III.1/HK/2026.

- Conflict of interest The authors declare no conflicts of interest.
- Ethics approval and consent to participate An AI-assisted language editing tool was used only to improve English clarity, consistency, and formatting. The authors reviewed and approved the final manuscript and remain fully responsible for all scientific content.
- Consent for publication Not applicable.
- Data, materials and code availability The reduced-order datasets and CFD post-processing tables will be available from the corresponding author upon reasonable request. The final CFD coefficient values should be inserted in Tables 6 and 7 before submission.
- Author contribution Conceptualization, A.S., F.H., and A.M.; methodology, A.S., A.M., and F.H.; CFD workflow and post-processing, A.S., A.Y., N.P., D.H., A.Sep., and I.R.A.F.; validation planning, A.S., F.H., and A.M.; writing-original draft preparation, A.S.; writing-review and editing, S.T.P., D.T., A.C., R.K., N.R.; supervision, F.H. and A.M.; project administration, A.S., and D.S. All authors have read and agreed to the submitted version of the manuscript.

References

[1] Abu Salem, K., Palaia, G., Bravo-Mosquera, P.D., Quarta, A.A.: A review of

novel and non-conventional propulsion integrations for next-generation aircraft. Designs **8**, 20 (2024) https://doi.org/10.3390/designs8020020

[2] Yu, F., *et al.*: A review of hybrid-electric propulsion in aviation: Modeling methods, energy management strategies, and future prospects. Aerospace **12**, 895 (2025) https://doi.org/10.3390/aerospace12100895

[3] Zhang, J., Roumeliotis, I., Zolotas, A.: Sustainable aviation electrification: A comprehensive review of electric propulsion system architectures, energy management, and control. Sustainability **14**, 5880 (2022) https://doi.org/10.3390/su14105880

[4] Borer, N.K., Reynolds, J.R., Wallace, R.D.: Flight performance maneuver planning for NASA's X-57 Maxwell flight demonstrator-part 2: Power-on effects. In: AIAA Aviation Forum (2024). https://doi.org/10.2514/6.2024-4133

[5] Denham, C.L., Patil, M., Roy, C.J., Alexandrov, N.: Application of framework for estimating performance and associated uncertainty for modified aircraft configurations using NASA's X-57 Maxwell. In: AIAA SciTech Forum (2023). https://doi.org/10.2514/6.2023-2249

[6] Jayanti, E.B., *et al.*: Validation of a small UAV dynamic model using CFD and flight test data. Periodica Polytechnica Transportation Engineering **54**, 88–104 (2025) https://doi.org/10.3311/pptr.41190

[7] Casagrande Hirono, F., Torija, A.J., Grimshaw, S.D., Cousins, D., Farman, J., Taylor, J.V.: Aerodynamic and aeroacoustic design of electric ducted fans. Aerospace Science and Technology **153**, 109411 (2024) https://doi.org/10.1016/j.ast.2024.109411

[8] Li, G., Song, H., Mao, S.: Research on the influence of ducted fan position on the performance of powered high-lift system. In: Journal of Physics: Conference Series, vol. 2820, p. 012063 (2024). https://doi.org/10.1088/1742-6596/2820/1/012063

[9] Maldonado, V., Fernandes, G.D.: Impact of blade shape on the aerodynamic performance and turbulent jet dynamics produced by a ducted rotor. Physics of Fluids **36** (2024) https://doi.org/10.1063/5.0207621

[10] Mao, S., *et al.*: Optimization design of the ducted fan powered high-lift system based on i-sight platform. In: Journal of Physics: Conference Series, vol. 2808, p. 012049 (2024). https://doi.org/10.1088/1742-6596/2808/1/012049

[11] Su, B., *et al.*: Study on lift enhancement for upper surface blowing system with electric ducted fan. In: IET Conference Proceedings, vol. 2020, pp. 7–11 (2021). https://doi.org/10.1049/icp.2021.0274

[12] Wang, J., Zhang, X., Lu, J., Tang, Z.: Numerical simulation and experimental study on the aerodynamics of propulsive wing for a novel electric VTOL aircraft. Aerospace **11**, 431 (2024) https://doi.org/10.3390/aerospace11060431

[13] Wei, J., Lu, B., Zha, Z., Li, Q.: Aerodynamic modeling of a distributed propulsion system with coupling between propellers, wing, and flaps. Aerospace Science and Technology **166**, 110521 (2025) https://doi.org/10.1016/j.ast.2025.110521

[14] Weinstein, R., Spada, V.A., Simmons, B.M.: Experimental study of aero-propulsive interactions for electric ducted fan arrays in multiple positions on a wing. In: AIAA SciTech Forum (2025). https://doi.org/10.2514/6.2025-1484

[15] Xia, J., Zhou, Z.: The modeling and control of a distributed-vector-propulsion UAV with aero-propulsion coupling effect. Aerospace **11**, 284 (2024) https://doi.org/10.3390/aerospace11040284

[16] Yang, X., Liu, T., Jia, W.: Research on the aerodynamic-propulsion coupling characteristics of a distributed propulsion system. Applied Sciences **15**, 3536 (2025) https://doi.org/10.3390/app15073536

[17] Zhang, X., *et al.*: Experimental research on aero-propulsion coupling characteristics of a distributed electric propulsion aircraft. Chinese Journal of Aeronautics **36**, 201–212 (2022) https://doi.org/10.1016/j.cja.2022.12.008

[18] Zhao, X., *et al.*: Research on conceptual design method and propulsive/aerodynamic coupling characteristics of DEP STOL UAV. Drones **9**, 363 (2025) https://doi.org/10.3390/drones9050363

[19] Zhao, Y., Tian, Y., Wan, Z.: Longitudinal aerodynamic characteristics of ducted fan propelled fixed-wing VTOL aircraft hovering in ground effect. Aerospace **10**, 659 (2023) https://doi.org/10.3390/aerospace10080659

[20] Zong, J., *et al.*: Design and modeling of a high-peak-power distributed electric propulsion system for a super-STOL UAV. Drones **8**, 761 (2024) https://doi.org/10.3390/drones8120761

[21] Kim, D., *et al.*: Aerodynamic analysis and static stability analysis of manned/unmanned distributed propulsion aircraft using actuator methods. Journal of Wind Engineering and Industrial Aerodynamics **214**, 104648 (2021) https://doi.org/10.1016/j.jweia.2021.104648

[22] Mardanpour, P., Richards, P.W., Nabipour, O., Hodges, D.H.: Effect of multiple engine placement on aeroelastic trim and stability of flying wing aircraft. Journal of Fluids and Structures **44**, 67–86 (2013) https://doi.org/10.1016/j.jfluidstructs.2013.09.018

[23] Montano, F., Dimino, I., Milazzo, A.: A preliminary evaluation of morphing horizontal tail design for UAVs. Aerospace **11**, 266 (2024) https://doi.org/10.3390/aerospace11040266

[24] Sadraey, M.: Aircraft Design: A Systems Engineering Approach. Wiley, Hoboken, NJ, USA (2013)

[25] Sadraey, M.: Automatic Flight Control Systems. Synthesis Lectures on Mechanical Engineering. Morgan & Claypool, ??? (2020). https://doi.org/10.2200/s00968ed1v01y201911mec023

[26] Chen, S., Guo, Z., Liu, D., Hu, D., Zhu, B.: Aerodynamic optimization of wings under slipstream effects for a distributed propulsion system. Aerospace Science and Technology, 111929 (2026) https://doi.org/10.1016/j.ast.2026.111929

[27] Da Silva Filho, R.R., De Souza Papini, G.: Numerical analysis of pressure distribution in a low aspect ratio wing with distributed electric propulsion. Journal of the Brazilian Society of Mechanical Sciences and Engineering **43** (2021) https://doi.org/10.1007/s40430-021-02892-y

[28] Jin, Y., Qian, Y., Zhang, Y., Zhuge, W.: Modeling of ducted-fan and motor in an electric aircraft and a preliminary integrated design. SAE International Journal of Aerospace **11**, 115–126 (2018) https://doi.org/10.4271/01-11-02-0007

[29] Chen, Z., Liu, D., Hou, Z., Chen, S.: Mission-oriented propulsion system configuration and whole aircraft redundancy safety performance for distributed electric propulsion UAVs. Drones **9**, 662 (2025) https://doi.org/10.3390/drones9090662

[30] Satria Palar, P., Nguyen Van, E., Bartoli, N., Morlier, J.: Design exploration of a distributed electric propulsion aircraft using explainable surrogate models. Journal of Aircraft **61**, 967–982 (2024) https://doi.org/10.2514/1.C037323

[31] De Paola, E., Camussi, R., Stoica, G.L., Di Marco, A., Capobianchi, G.: Aerodynamic and aeroacoustic experimental investigation of a three-propellers DEP configuration. Aerospace Science and Technology **154**, 109508 (2024) https://doi.org/10.1016/j.ast.2024.109508

[32] Deere, K.A., *et al.*: Computational component build-up for the X-57 Maxwell distributed electric propulsion aircraft. In: AIAA SciTech Forum (2018). https://doi.org/10.2514/6.2018-1275

Editorial Policies for:

Springer journals and proceedings: https://www.springer.com/gp/editorial-policies

Nature Portfolio journals: https://www.nature.com/nature-research/editorial-policies

Scientific Reports: https://www.nature.com/srep/journal-policies/editorial-policies

BMC journals: https://www.biomedcentral.com/getpublished/editorial-policies

Appendix A Extended Data

A.1 Geometry and Reference Quantities

Table A1 Full wing configuration retained from the LSU 05 NG dataset.

Parameter	Symbol	Value	Unit
Mean takeoff mass	m_{TO}	102	kg
Main wing span	b_w	5.5	m
Wing root chord	$c_{r,w}$	0.73	m
Wing tip chord	$c_{t,w}$	0.44	m
Wing taper ratio	λ_w	0.603	-
Wing planform area	S_w	3.45	m^2
Wing aspect ratio	AR_w	8.769	-
Maximum lift coefficient	$C_{L,\max}$	2.5	-
Mean aerodynamic chord	MAC	0.642	m
Wing lift-curve slope	$C_{L_{\alpha,w}}$	0.1	1/rad
Wing airfoil	-	FX 76-MP-160	-

Table A2 Tail configuration retained from the LSU 05 NG dataset.

Parameter	Symbol	Value	Unit
HTP span	b_{HTP}	1.5	m
HTP root chord	$c_{r,\mathrm{HTP}}$	0.44	m
HTP tip chord	$c_{t,\mathrm{HTP}}$	0.44	m
HTP taper ratio	λ_{HTP}	1.0	-
HTP planform area	S_{HTP}	0.6603	m^2
HTP aspect ratio	AR_{HTP}	3.4	-
HTP quarter-chord sweep	$\Lambda_{0.25c,\mathrm{HTP}}$	0	deg
HTP leading-edge sweep	$\Lambda_{\mathrm{LE,HTP}}$	0	deg
HTP airfoil	-	NACA 0012	-
VTP span	b_{VTP}	0.5	m
VTP root chord	$c_{r,\mathrm{VTP}}$	0.44	m
VTP tip chord	$c_{t,\mathrm{VTP}}$	0.204	m
VTP taper ratio	λ_{VTP}	0.46	-
VTP planform area	S_{VTP}	0.1610	m^2
VTP aspect ratio	AR_{VTP}	1.6	-
VTP quarter-chord sweep	$\Lambda_{0.25c,\mathrm{VTP}}$	40	deg
VTP leading-edge sweep	$\Lambda_{\mathrm{LE,VTP}}$	37	deg
VTP airfoil	-	NACA 0012	-

For a symmetric wing, the reference planform quantities are reconstructed from the chord distribution c(y) as

$S_w = 2\int_0^{b/2} c(y)\,dy, \qquad AR_w = \frac{b^2}{S_w}, \qquad \mathrm{MAC} = \frac{\int_0^{b/2} c^2(y)\,dy}{\int_0^{b/2} c(y)\,dy}$

The normalized spanwise coordinate is $\eta = \frac{y}{b/2}$

A.2 EDF placement and propulsion parameters

Table A3 DEP-EDF design configuration.

Parameter	Symbol	Value	Unit/note
EDF units per semi-span	$N_{\mathrm{EDF},1/2}$	6	-
Total EDF units	N_{EDF}	12	-
EDF diameter	D_{EDF}	70	mm
EDF radius	R_{EDF}	35	mm
EDF exit area	A_{EDF}	3846.5	mm^2
Motor efficiency	η_m	92	%
Fan efficiency	η_f	80	%
Spanwise corridor	η_j	0.15-0.85	semi-span fraction
Near-TE chordwise band	$x_j/c(y_j)$	0.60-0.90	local-chord fraction
Slipstream empirical factor	k_j	0.7	-
Effective slipstream radius	σ_j	$1.2R_{\mathrm{EDF}}$	approximately 42 mm
Exit velocity ratio	$V_{\mathrm{exit}}/V_\infty$	2.0	-
Induced jet velocity constant	k_{ind}	1.15	-
Wing airfoil data	-	FX 76-MP-160 polar	-
Tail airfoil data	-	NACA 0012 polar	-

Table A4 Initial semi-span EDF stations.

EDF station	y_j (mm)	η_j	Representative local chord $c(y_j)$ (m)	Comment
1	412.5	0.150	0.687	Inboard boundary of placement corridor
2	772.5	0.281	-	Uniform-spacing initial design
3	1132.5	0.412	-	Uniform-spacing initial design
4	1492.5	0.543	-	Uniform-spacing initial design
5	1852.5	0.674	-	Uniform-spacing initial design
6	2212.5	0.805	0.497	Outboard station below 0.85 limit

The chordwise EDF location is no longer reported as undefined. It is treated as a bounded near-trailing-edge design variable:

$$0.60 \leq \frac{x_j}{c(y_j)} \leq 0.90$$

This band preserves the intended near-trailing-edge placement while avoiding an unresolved entry in the manuscript.

A.3 Detailed reduced-order equations

The local effective velocity is

$$V_{\mathrm{eff}}(y) = V_\infty + \Delta V_{\mathrm{slip}}(y)$$

The dynamic pressure and lift per unit span are

$$q_{\mathrm{loc}}(y) = \frac{1}{2}\rho V_{\mathrm{eff}}^2(y), \qquad L'(y) = q_{\mathrm{loc}}(y)\, c(y)\, c_l(y)$$

The Gaussian superposition model is

$$\Delta V_{\mathrm{slip}}(y) = \sum_{j=1}^{N_{\mathrm{EDF}}} \Delta V_j \exp\left(-\frac{(y-y_j)^2}{2\sigma_j^2}\right)$$

When thrust is inserted explicitly,

$$\Delta V_j = k_j \sqrt{\frac{2T_j}{\rho A_j}}$$

The full-wing lift coefficient is

$$C_L = \frac{2}{q_\infty S_w} \int_0^{b/2} q_{\mathrm{loc}}(y)\, c(y)\, c_l(y)\, dy$$

The induced-drag contribution is represented conceptually as

$$C_{D_i} = \frac{C_L^2}{\pi e A R_w}$$

where the effective Oswald factor e is reduced when the slipstream load distribution departs from the ideal elliptical loading. The total drag coefficient is

$$C_D = C_{D_0} + C_{D_i}$$

The thrust produced by the j-th EDF is estimated from a momentum representation:

$$T_j = \rho A_j V_{\mathrm{exit},j}(V_{\mathrm{exit},j} - V_\infty)$$

The corresponding shaft-power estimate used in the reduced-order model is

$$P_j = \frac{T_j V_{\mathrm{exit},j}}{\eta_{m,j}\eta_{f,j}}$$

The total thrust and power are

$$T_{\mathrm{DEP}} = \sum_{j=1}^{N_{\mathrm{EDF}}} T_j, \qquad P_{\mathrm{DEP}} = \sum_{j=1}^{N_{\mathrm{EDF}}} P_j$$

A compact pressure-increment expression for a near-trailing-edge EDF jet is

$$\Delta p(x) = \rho\left(\left(V_\infty + \sqrt{\frac{2T_j}{\rho A_j}}\exp\left(-\frac{(x-x_j)^2}{2\sigma_x^2}\right)\right) - V_\infty^2\right)$$

The corresponding incremental pitching moment about the CG is

$$\Delta C_M = \frac{1}{q_\infty c^2}\int_0^c \Delta p(x)(x - x_{\mathrm{CG}})\,dx$$

The main manuscript uses the compact trim equation because the central result is the elevator-authority margin:

$$C_M = C_{M_0} + C_{M_\alpha}\alpha + C_{M_{C_L}}C_L + C_{M_{\delta_e}}\delta_e$$

A.4 CFD angle-of-attack design-support assessment

This section replaces the earlier wording that described CFD as direct verification. The CFD model is a representative three-EDF wing-DEP model used to document geometry-resolved aerodynamic and rotor diagnostics. It supports the design interpretation but does not validate the twelve-EDF reduced-order model one-to-one.

Table A5 CFD fixed input parameters.

Parameter	Symbol	Value	Unit/note
Wing CFD reference area	$S_{w,\mathrm{CFD}}$	2.0895×10^5	mm^2
Wing CFD reference area	$S_{w,\mathrm{CFD}}$	0.20895	m^2
EDF diameter	D	70	mm
EDF rotor-blade assembly surface area	-	10538	mm^2 per EDF
Number of EDFs	$N_{\mathrm{EDF,CFD}}$	3	-
Freestream speed	V_∞	15	m/s
Rotor speed, power-on	rpm	35000	rev/min
Rotor speed, power-on	n	583.333	rev/s
Power-off condition	-	Rotor motion disabled	baseline wing/wing-only reference
Power-on condition	-	Three rotors active	powered DEP case

Table A6 CFD angle-of-attack operating matrix.

Case ID	α (deg)	Power-off condition	Power-on condition
CFD-01	0	$V_\infty = 15$ m/s; rotors off	$V_\infty = 15$ m/s; 3 EDFs at 35000 rpm
CFD-02	5	$V_\infty = 15$ m/s; rotors off	$V_\infty = 15$ m/s; 3 EDFs at 35000 rpm
CFD-03	10	$V_\infty = 15$ m/s; rotors off	$V_\infty = 15$ m/s; 3 EDFs at 35000 rpm
CFD-04	12	$V_\infty = 15$ m/s; rotors off	$V_\infty = 15$ m/s; 3 EDFs at 35000 rpm
CFD-05	15	$V_\infty = 15$ m/s; rotors off	$V_\infty = 15$ m/s; 3 EDFs at 35000 rpm
CFD-06	17	$V_\infty = 15$ m/s; rotors off	$V_\infty = 15$ m/s; 3 EDFs at 35000 rpm
CFD-07	19	$V_\infty = 15$ m/s; rotors off	$V_\infty = 15$ m/s; 3 EDFs at 35000 rpm
CFD-08	20	$V_\infty = 15$ m/s; rotors off	$V_\infty = 15$ m/s; 3 EDFs at 35000 rpm

The CFD force coefficients are obtained from

$$q_\infty = \frac{1}{2}\rho V_\infty^2,$$

$$C_{L,\mathrm{CFD}} = \frac{F_y}{q_\infty S_{w,\mathrm{CFD}}}, \qquad C_{D,\mathrm{CFD}} = \frac{|F_z|}{q_\infty S_{w,\mathrm{CFD}}}, \qquad C_{S,\mathrm{CFD}} = \frac{F_x}{q_\infty S_{w,\mathrm{CFD}}}, \qquad L/D = \frac{F_y}{|F_z|}$$

The three-EDF aggregate outputs are

$$T_\Sigma = T_1 + T_2 + T_3, \qquad Q_\Sigma = Q_1 + Q_2 + Q_3, \qquad \dot{m}_\Sigma = \dot{m}_1 + \dot{m}_2 + \dot{m}_3$$

Rotor coefficients are reported using the EDF diameter D and rotor speed n=rpm/60:

$$C_T = \frac{T}{\rho n^2 D^4}, \qquad C_Q = \frac{Q}{\rho n^2 D^5}, \qquad C_P = \frac{P}{\rho n^3 D^5} = 2\pi C_Q$$

The total diagnostic shaft power is

$$P_{\mathrm{shaft},\Sigma} = 2\pi n \sum_{j=1}^{3} |Q_j|$$

A.5 Additional reduced-order figures

A.6 Code workflow and reproducibility checklist

1. Load wing and tail reference geometry, including b_w, S_w, MAC, tail reference areas, and airfoil polar data.

2. Define reduced-order flight regimes: cruise, takeoff, landing, and stall using $V_\infty and \alpha$.

3. Define EDF parameters: $N_{EDF}, D_{EDF}, A_{EDF}, \eta_m, \eta_f, k_j, \sigma_j, V_{\text{exit}}/V_\infty$, and kind.

4. Construct the spanwise grid and interpolate c(y) and polar values.

5. Compute baseline sectional lift and drag.

6. Compute EDF thrust, power, $\Delta V_{slip}, and V_{eff}$.

7. Integrate $C_L and C_D$ over the semi-span.

8. Compute $C_M, \delta_{e,trim}, and M_\delta for each x_{CG}/MAC$ case.

9. For CFD support, export power-off and power-on forces, thrust, torque, mass flow, and power for all eight angles of attack.

10. Report CFD values (power off CFD outputs, power on CFD aerodynamic outputs, power on CFD aggregate EDF outputs, individual EDF outputs for thrust, torque and mass flow, and power on minus power off diagnostic comparisons) and avoid describing the results as formal validation unless matched experimental data are available.

A.7 Full reduced-order numerical results

Table A7 Lift-coefficient augmentation retained from the reduced-order DEP analysis.

No.	Case	V_∞ (m/s)	α (deg)	x_{CG}/MAC	$C_{L,0}$	$C_{L,\text{DEP}}$	Lift gain (%)
1	Cr.	25	3	0.30	0.804	1.288	60.2
2	TO	22	8	0.30	0.981	1.509	53.8
3	LD	21	9	0.30	1.079	1.636	51.6
4	ST	19	17	0.30	1.415	2.080	47.0
5	Cr.	25	3	0.35	0.818	1.309	60.0
6	TO	22	8	0.35	0.981	1.535	56.5
7	LD	21	9	0.35	1.079	1.662	54.0
8	ST	19	17	0.35	1.415	2.080	47.0
9	Cr.	25	3	0.37	0.824	1.318	60.0
10	TO	22	8	0.37	0.981	1.545	57.5
11	LD	21	9	0.37	1.078	1.673	55.2
12	ST	19	17	0.37	1.415	2.080	47.0

Table A8 Drag and efficiency consequences of the same DEP cases.

No.	Case	x_{CG}/MAC	$C_{D,0}$	$C_{D,DEP}$	Drag inc. (%)	$(C_L/C_D)_0$	$(C_L/C_D)_{DEP}$	Change (%)
1	Cr.	0.30	0.045	0.086	91.1	17.869	14.984	-16.15
2	TO	0.30	0.071	0.139	95.8	13.799	10.824	-21.56
3	LD	0.30	0.081	0.163	101.2	13.290	10.058	-24.32
4	ST	0.30	0.149	0.282	89.3	9.497	7.391	-22.18
5	Cr.	0.35	0.044	0.086	95.5	18.724	15.303	-18.27
6	TO	0.35	0.071	0.137	93.0	13.799	11.232	-18.60
7	LD	0.35	0.081	0.160	97.5	13.290	10.406	-21.70
8	ST	0.35	0.149	0.282	89.3	9.497	7.391	-22.18
9	Cr.	0.37	0.043	0.086	100.0	19.051	15.398	-19.17
10	TO	0.37	0.071	0.136	91.5	13.799	11.380	-17.53
11	LD	0.37	0.081	0.159	96.3	13.290	10.540	-20.69
12	ST	0.37	0.149	0.281	88.6	9.497	7.391	-22.18

Table A9 Pitching-moment coefficients retained from the trim analysis.

No.	Case	x_{CG}/MAC	$C_{M,0}$	$C_{M,DEP}$
1	Cr.	0.30	0	0
2	TO	0.30	-0.187	0.00555
3	LD	0.30	-0.248	-0.006
4	ST	0.30	-0.897	-0.606
5	Cr.	0.35	0	0.00347
6	TO	0.35	-0.134	0.00278
7	LD	0.35	-0.191	0
8	ST	0.35	-0.827	-0.502
9	Cr.	0.37	-0.00833	0.00694
10	TO	0.37	-0.112	-0.00278
11	LD	0.37	-0.168	0.00278
12	ST	0.37	-0.799	-0.46

Table A10 Elevator trim and residual authority.

No.	Case	x_{CG}/MAC	$\delta_{e,0}$ (deg)	$\delta_{e,DEP}$ (deg)	M_δ (deg)	Status
1	Cr.	0.30	-13.60	-3.84	21.15	OK
2	TO	0.30	-24.99	-22.91	2.08	OK
3	LD	0.30	-24.99	-24.99	0.00	Limit
4	ST	0.30	-24.99	-24.99	0.00	Limit
5	Cr.	0.35	-11.63	-0.07	24.92	OK
6	TO	0.35	-24.99	-18.95	6.04	OK
7	LD	0.35	-24.99	-20.72	4.27	OK
8	ST	0.35	-24.99	-24.99	0.00	Limit
9	Cr.	0.37	-10.83	1.43	23.56	OK
10	TO	0.37	-24.99	-17.54	7.45	OK
11	LD	0.37	-24.99	-19.19	5.80	OK
12	ST	0.37	-24.99	-24.99	0.00	Limit

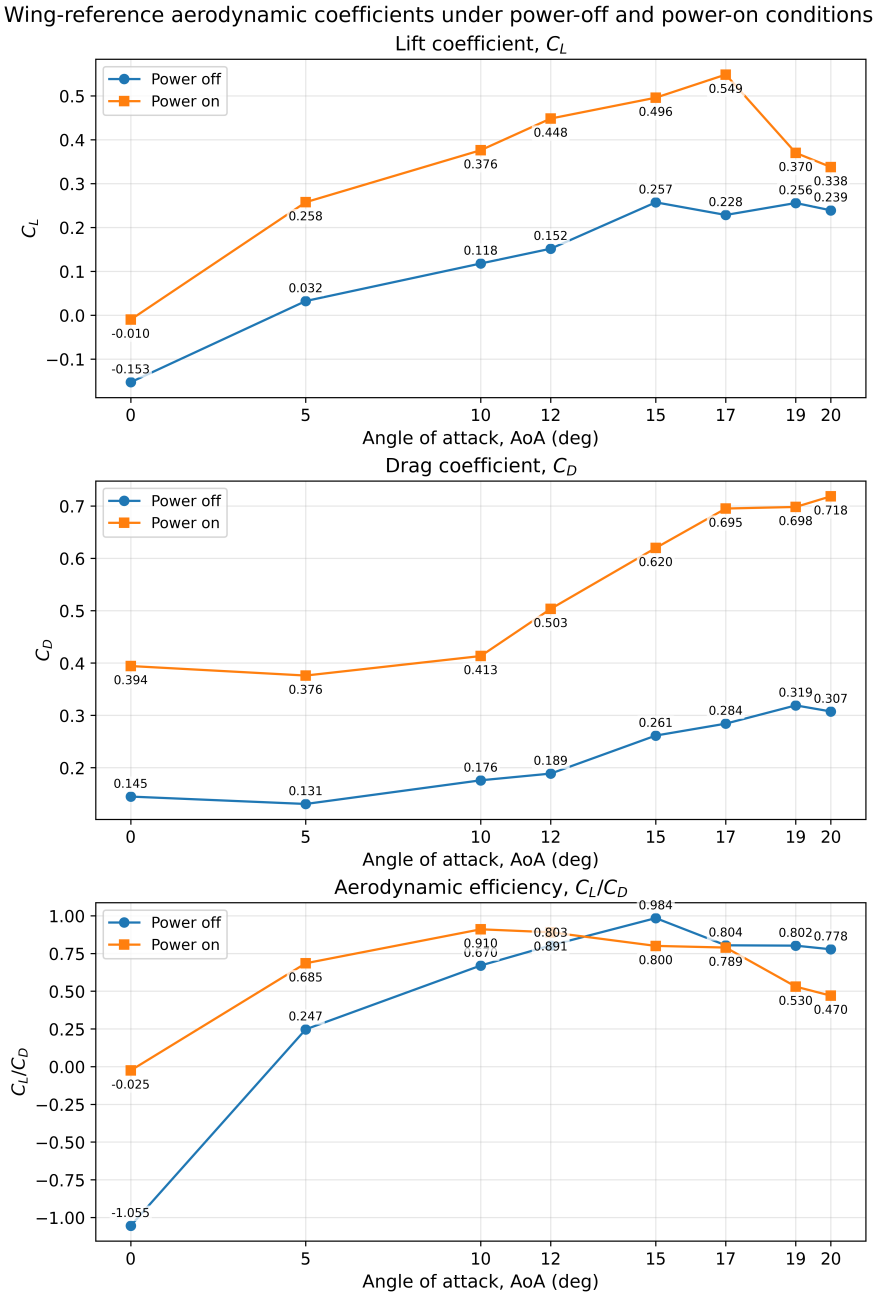


Fig. 6 Wing-reference aerodynamic coefficients in paired power-off and power-on conditions. The coefficient trends show that DEP provides the largest aerodynamic return at low AoA and a progressively weaker benefit as the wing approaches the high-lift and near-stall regime.

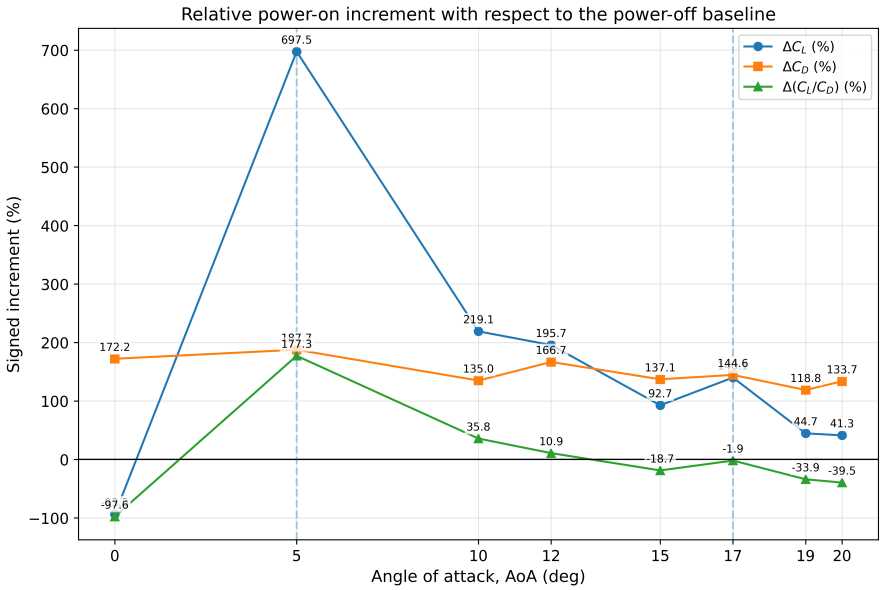


Fig. 7 Signed power-on increments relative to the power-off baseline. The largest positive efficiency change occurs at $\alpha = 5°$, whereas the efficiency increment becomes essentially zero and slightly negative at $\alpha = 17°$, which marks the onset of diminishing aerodynamic return.

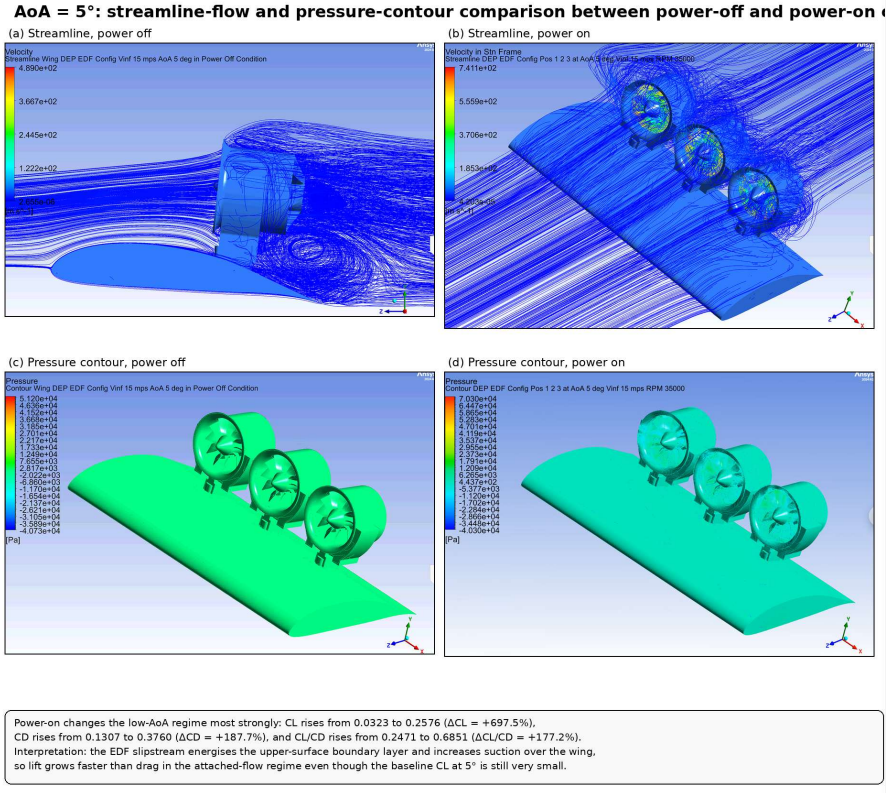


Fig. 8 Streamline-flow and pressure-contour comparison at $\alpha = 5°$. The power-on case demonstrates that the slipstream intensifies local loading and improves attached-flow behaviour, which is consistent with the very large positive increments in C_L and C_L/C_D.

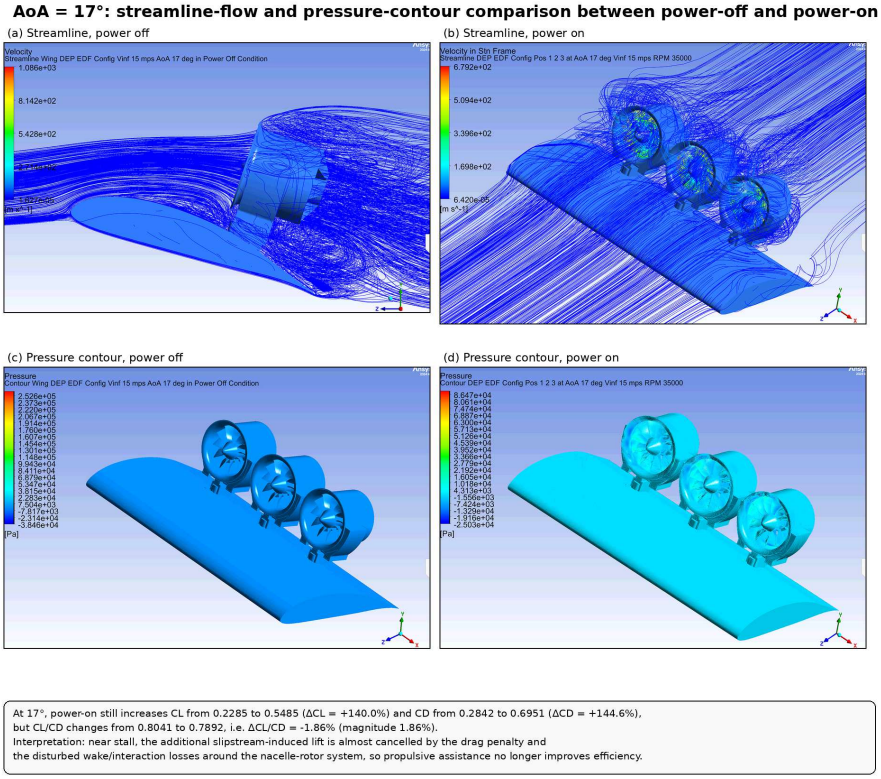


Fig. 9 Streamline-flow and pressure-contour comparison at $\alpha = 17°$. Although DEP still increases C_L, the near-stall flow field shows that the accompanying drag growth and interaction losses suppress any meaningful efficiency gain.

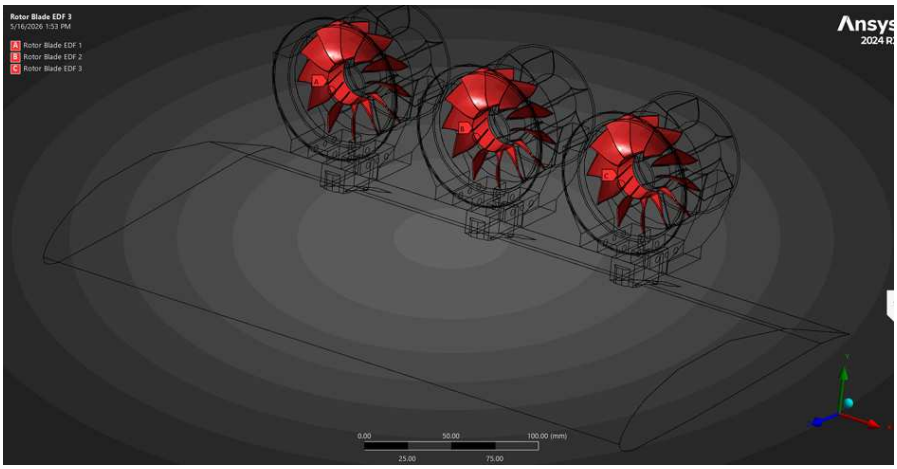


Fig. A1 CFD power-on model with three 70 mm EDFs installed on the LSU 05 NG wing model.

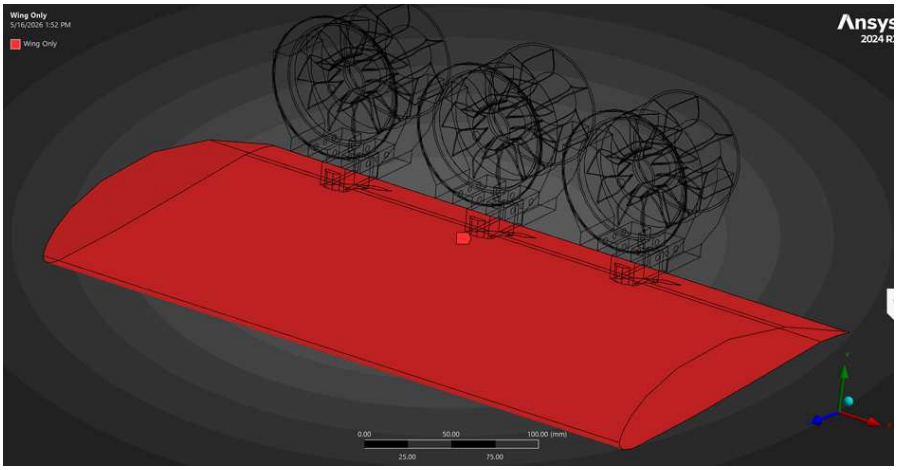


Fig. A2 CFD power-off/wing-only reference model.

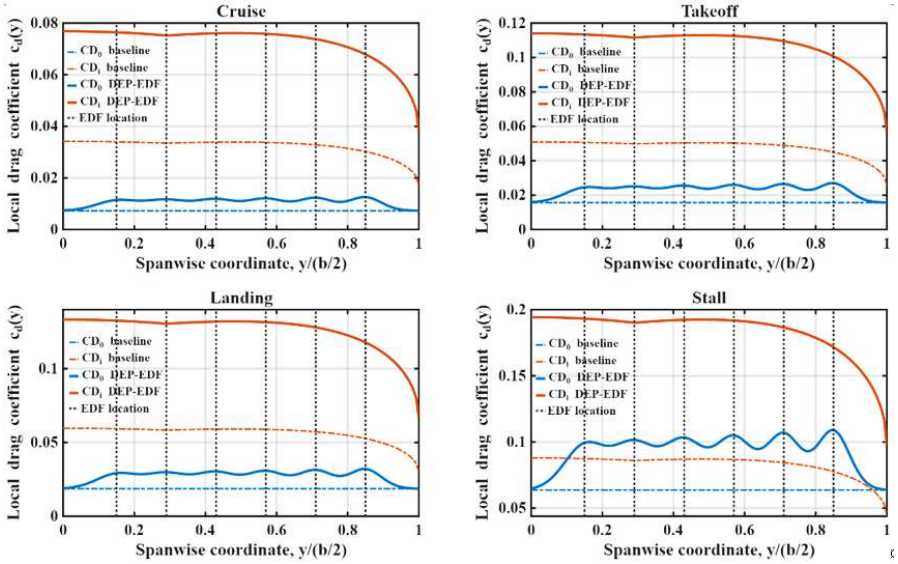


Fig. A3 Spanwise local drag coefficient distribution showing the profile and induced-drag penalty caused by DEP slipstream loading.

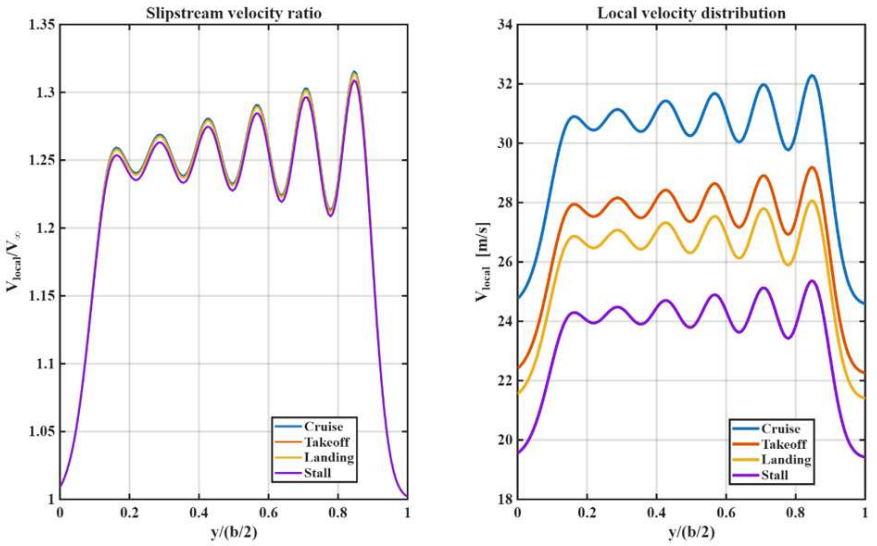


Fig. A4 Slipstream velocity ratio and local velocity field used in the reduced-order analysis.

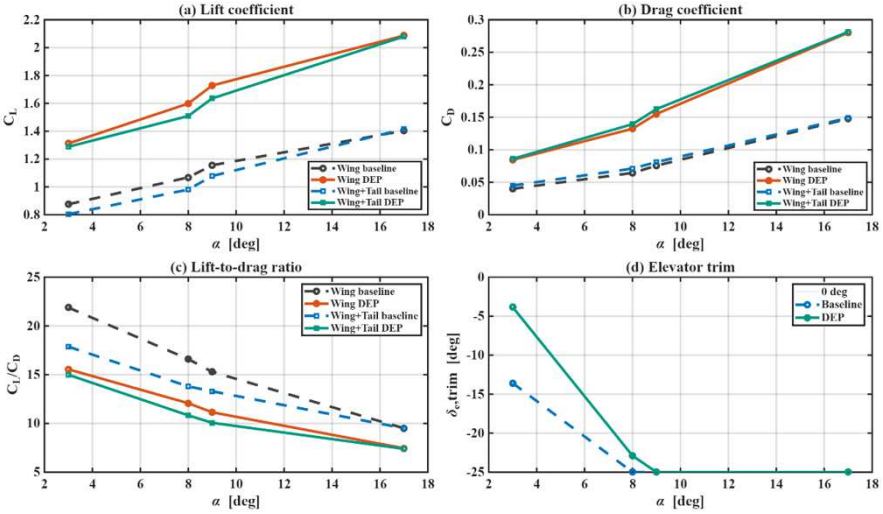


Fig. A5 Aircraft-level lift, drag, efficiency, and elevator-trim response.